Engineering Geology 241 (2018) 86–96

Contents lists available at ScienceDirect

Engineering Geology

journal homepage: www.elsevier.com/locate/enggeo

Quantifying the impact of dry debris flow against a rigid barrier by DEM analyses

Weigang Shen[a], Tao Zhao[a,*], Jidong Zhao[b], Feng Dai[a], Gordon G.D. Zhou[c]

[a] State Key Laboratory of Hydraulics and Mountain River Engineering, College of Water Resource and Hydropower, Sichuan University, Chengdu 610065, China
[b] Department of Civil and Environmental Engineering, Hong Kong University of Science and Technology, Clear Water Bay, Kowloon, Hong Kong, China
[c] Institute of Mountain Hazards and Environment, Chinese Academy of Sciences, Ministry of Water Conservancy, Chengdu 610041, China

ARTICLE INFO

Keywords:
Debris flow
Rigid barrier
Discrete element method
Barrier slope
Impact force

ABSTRACT

This study investigates the interaction between dry debris flows and a rigid barrier through discrete element modeling (DEM) of flume tests. The debris materials were modeled as an assembly of loosely packed spherical particles and the rigid barrier was represented by a layer of fixed particles. The numerical model was validated by comparing the numerical results with the experimental data reported in the literature, in terms of the debris flow morphology and evolution of impact forces acting on the rigid barrier. This model was further employed to examine the influence of barrier slope on the debris-barrier interactions. Based on the numerical results, three interaction stages were identified, namely the frontal impact, run-up and pile-up. The maximum impact force measured in this study exhibits a power law dependence on the barrier slope. In addition, during the impact process, the majority of initial total energy was dissipated by particle-particle and particle-flume interactions, while only a negligibly small amount of energy was dissipated by particle-barrier interaction. The numerical results also indicate that long spreading debris flows are very effective in facilitating energy dissipation, diminishing the impact force acting on the rigid barrier. These considerations can finally contribute to the design of effective debris flow barriers.

1. Introduction

Debris flows are rapid solid mass movements in which a mixture of loose soil, rock, organic matter, air and water are mobilized to flow downslope. They are also called granular flows because of the granular nature of the involved solid materials (Law, 2015). Due to the high mobility and huge entrained solid volume, debris flows can always pose significant hazards to human lives, infrastructures and lifeline facilities worldwide, threatening populated areas located even far away from the slope source region (Legros, 2002; Hürlimann et al., 2006; Liu et al., 2014; Chen et al., 2015; Gao et al., 2017; Fan et al., 2018). Thus, protective structures like rigid barriers are widely constructed to mitigate such destructive hazards. In these cases, the estimation of the maximum impact force exerted by debris flows is always a prerequisite parameter for barrier design.

In engineering practices, several semi-empirical methods have been used to estimate the maximum impact force of debris flows acting on a rigid barrier, such as hydrostatic approach, shock wave approach and hydrodynamic approach. These methods calculate the impact force based on the peak debris flow velocity and flow thickness, which are estimated by some widely accepted debris mobility models such as DAN-W (Hungr, 1995) and 2d-DMM (Kwan and Sun, 2006). Nevertheless, these available methods still have the difficulty in reconciling theoretical concepts with field and experimental observations and thus would possibly lead to high discrepancies (Koo et al., 2017). As a result, none of them have been acknowledged as a universal formula for estimating the impact force of debris flow on rigid barriers. This is because each method was obtained in specific impacting and boundary conditions with strong assumptions, such that they cannot be generalized for wider applications. In addition, these methods fail to consider the influence of debris-barrier interaction (Koo et al., 2017). Koo et al. (2017) investigated the debris-barrier interaction using laboratory flume tests and observed that during impact, the maximum momentum of a debris flow was 30% lower than the testing results without considering the debris-barrier interactions. Ng et al. (2017b) investigated the impacting process of the debris flow on a rigid barrier using geotechnical centrifuge testing. They concluded that the debris-barrier interaction can facilitate the dissipation of energy in the flowing solid mass. Thus, it is worthwhile to highlight the importance of debris-barrier interactions in barrier design.

The dynamic interaction between debris flow and a rigid barrier are very complicated because it depends on the kinematics of debris flows

* Corresponding author.
E-mail addresses: wgshen@stu.scu.edu.cn (W. Shen), zhaotao@scu.edu.cn (T. Zhao), jzhao@ust.hk (J. Zhao), fengdai@scu.edu.cn (F. Dai), gordon@imde.ac.cn (G.G.D. Zhou).

https://doi.org/10.1016/j.enggeo.2018.05.011
Received 5 December 2017; Received in revised form 8 May 2018; Accepted 8 May 2018
Available online 09 May 2018
0013-7952/

(e.g. solid mass and velocity), mechanical characteristics of soil, the stiffness and geometrical characteristics of the barrier (Brighenti et al., 2013; Jiang and Towhata, 2013; Choi et al., 2015; Jiang et al., 2015; Song et al., 2016). The dynamic motion of debris flows can always lead to large deformation, displacement, as well as energy transformation and dissipation, which in turn change the debris-barrier interactions. In the literature, the debris-barrier interactions have been addressed by several laboratory flume tests (Moriguchi et al., 2009; Jiang and Towhata, 2013; Jiang et al., 2015; Song et al., 2016; Koo et al., 2017). Brighenti et al. (2013) and Ashwood and Hungr (2016) investigated the interaction between debris flow and a flexible barrier. Their results indicate that the deflection of the flexible barrier can prolong the duration of debris-barrier interaction. Such long interaction duration can effectively reduce the peak impact force. Moriguchi et al. (2009) investigated the influence of slope angle on debris-barrier interactions and concluded that the impact force increases with the slope angle. Jiang and Towhata (2013) investigated the debris-barrier interaction through a series of experiments on dry debris flow impacting a rigid barrier. They found that the impact force consists of debris drag force, gravitational and frictional forces and passive earth force. Jiang et al. (2015) investigated the influence of particle characteristics on the impact process of a debris flow. They concluded that the particle characteristics can dramatically influence the impact force by changing the flow deposition morphology behind the barrier. Song et al. (2016) investigated the influence of solid fraction of a debris flow on the debris-barrier interactions. They observed that the solid fraction can significantly influence the shape of debris deposition behind the barrier.

The debris-barrier interaction can also be addressed conveniently by the discrete element method (DEM) (Cundall and Strack, 1979; Gabrieli and Ceccato, 2016). The DEM has been widely used for numerical modeling of rock avalanches and debris flows (Calvetti et al., 2000; Salciarini et al., 2010; Shan and Zhao, 2014; Zhao et al., 2014; Zhao et al., 2016; Calvetti et al., 2017; Shen et al., 2017; Zhao et al., 2017b; Zhao et al., 2018). It is an appropriate tool for modeling debris flows because of the discrete nature of materials involved in these phenomena (Law, 2015). In addition, the energy evolutions can also be recorded through DEM simulations, while it is almost impossible to obtain such information from measurements in experiments (Utili et al., 2015; Zhao et al., 2017a). Albaba et al. (2015) and Wu et al. (2016) simulated the process of dry debris flow impacting a rigid wall using the DEM. In their analyses, the DEM has been found to be an efficient method for quantifying the dynamics of debris flow.

While the main stream DEM models use the circular or spherical particles, they are not commonly appeared for soil particles or gravels in debris flow. The use of spherical particles in DEM simulations will inevitably lead to a soil structure different from that of real natural soils with a reduced granular internal friction (Zhao et al., 2015; Gao and Meguid, 2018). However, through careful model calibrations, an assembly of spherical particles with proper mechanical and physical properties can still be used to simulate the behavior of debris flows (Plassiard and Donzé, 2010; Law, 2015). Therefore, in the present study, the spherical particles are considered as a reasonable initial proxy to study debris-barrier interactions. The objective is to reveal the detailed mechanism of debris-barrier interactions and quantify the impact parameters for barrier design.

2. DEM model of flume test

2.1. DEM theory

The open source DEM code ESyS-Particle (Wang and Mora, 2009) was employed to run all the simulations presented in this paper. In DEM, the granular materials are modeled as a collection of rigid spherical particles. The translational and rotational motions of each single particle are governed by the Newton's second law of motion as,

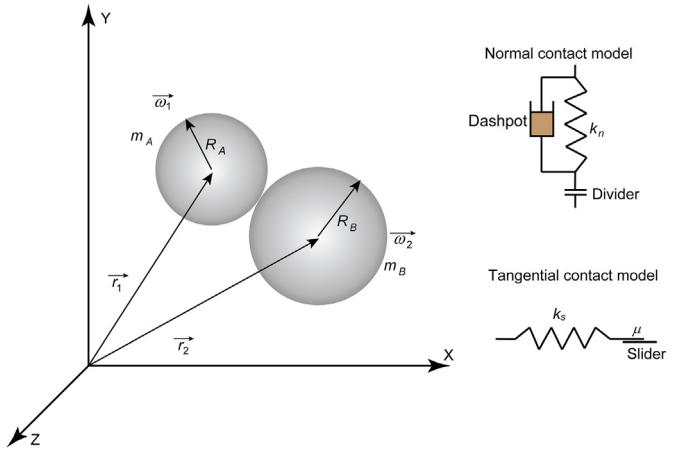

Fig. 1. The DEM contact model between two particles.

$$\overrightarrow{F_i} = m_i \frac{d^2}{dt^2}\overrightarrow{r_i} \tag{1}$$

$$\overrightarrow{T_i} = I_i \frac{d^2}{dt^2}\overrightarrow{\omega_i} \tag{2}$$

where $\overrightarrow{F_i}$ is the resultant force acting on particle i; $\overrightarrow{r_i}$ is the position of its centroid; m_i is the particle mass; $\overrightarrow{T_i}$ is the resultant moment acting on the particle; $\overrightarrow{\omega_i}$ is the angular velocity and I_i is the moment of inertia.

In DEM, the inter-particle interactions are computed by the cohesionless frictional model (CFM). This model consists of a linear elastic spring-dashpot model for the normal contacts and a Coulomb-like contact law for the tangential contacts (see Fig. 1). In order to replicate the energy dissipated by particle asperities being sheared off and the plastic deformations of the granular assembly, a linear viscous damping model (dashpot) is employed in the normal direction to dissipate a small amount of kinetic energy. The normal contact force (F_n) is calculated as,

$$F_n = k_n u_n + F_n^d \tag{3}$$

where u_n is the overlapping length between two particles in contact; k_n is normal contact stiffness and F_n^d is the normal damping force. The normal contact stiffness is defined as,

$$k_n = \pi E(R_A + R_B)/4 \tag{4}$$

where E is the particle Young's modulus; R_A and R_B are the radii of the two contacting particles.

The damping force (F_n^d) is calculated as,

$$F_n^d = 2\beta\sqrt{0.5(m_A + m_B)k_n}v_n \tag{5}$$

where β is the damping coefficient; m_A and m_B are the mass of the two contacting particles and v_n is the relative velocity between particles in the normal direction.

The tangential contact force at the current time step (F_s^n) is calculated incrementally as,

$$F_s^n = F_s^{n-1} + (\Delta F_s^{(1)} + \Delta F_s^{(2)}) \tag{6}$$

where F_s^{n-1} is the tangential contact force at the previous time step; $\Delta F_s^{(1)}$ and $\Delta F_s^{(2)}$ are the components of incremental tangential contact force, respectively. Here, $\Delta F_s^{(1)}$ results from the incremental tangential displacement (Δu_s), while $\Delta F_s^{(2)}$ is related to the rotation of particle contact plane. A detailed description of the algorithm to compute these two force components can be found in Wang and Mora (2009).

The magnitude of tangential force is limited by the following equation,

$$|F_s| \le \mu\ |F_n| \tag{7}$$

where μ is the coefficient of particle friction.

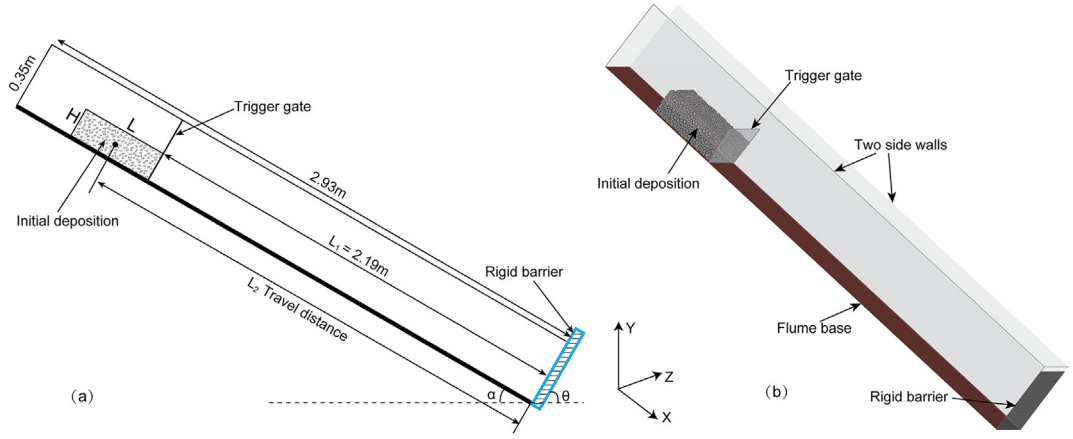

Fig. 2. (a) Sketch of the experimental flume (after Jiang and Towhata, 2013), (b) Numerical model configuration.

2.2. Model configuration

The numerical model configurations of flume test are set the same as those employed in the experimental tests by Jiang and Towhata, 2013 (see Fig. 2 (a) and (b)). The flume is 2.93 m in length, 0.3 m in width and 0.35 m in height. The slope angle (α) of the flume is 40°. The initial granular deposition has dimensions of L = 44 cm, H = 15 cm and width of 30 cm. The spreading distance of debris materials is defined as L_2. A rigid barrier, which is inclined at an angle of θ to the horizontal plane, is installed at the bottom end of the flume. The flume base and the rigid barrier are represented by a layer of fixed spherical particles with constant radii of 0.2 cm. The two lateral side walls are set frictionless as with the experiments in order to minimize the influence of boundary effects on the granular dynamics.

The initial debris deposition is composed of an assembly of 6993 randomly distributed poly-dispersed spherical particles. The particle size distribution (PSD) employed in this study is shown in Fig. 3 with the particle size ranging from 10 mm to 25 mm. In numerical simulations, the particles of size smaller than 10 mm were ignored because of their relatively low mass percentage in the initial granular sample (see Fig. 3). The input parameters of the DEM model are listed in Table 1.

In this study, the particle Young's modulus, Poisson's ratio and density are set according to the commonly used values in numerical simulations of granular medium, as listed in Table 1 (Salciarini et al., 2010; Law, 2015). The damping coefficient is set as 0.05 which was obtained by trial and error, so that the overall numerical results of debris dynamics can match the experimental observations in the model validation process. The friction coefficients of the debris particles (μ_1), the flume base (μ_2) and the rigid barrier (μ_3) are chosen according to the experimental observations in Jiang and Towhata, 2013. In all the simulations, the debris flow is initiated by instantaneous removal of the top trigger gate. Then, the granular mass would slide under gravity downwards the flume with confined motions by the two side walls. At the bottom end of the flume, the granular mass is arrested by the rigid barrier. The simulation lasts around 12 hr on a standard desktop computer (Intel® Core™ i7 CPU, 4.00 GHz × 8, and 16 GB RAM).

Table 1
Input parameters used in the DEM simulations.

DEM parameters	Value	DEM parameters	Value
Debris particle radius, r (mm)	5–12.5	Debris particle friction coefficient, μ_1	1.327
Debris particle density, ρ (kg/m^3)	2500	Flume friction coefficient, μ_2	0.466
Young's modulus of particle, E (MPa)	1×10^2	Barrier friction coefficient, μ_3	0.384
Particle Poisson's ratio, υ	0.25	Gravitational acceleration, g (m/s^2)	9.81
Viscous damping coefficient, β	0.05	Time step size, Δt (s)	1×10^{-6}

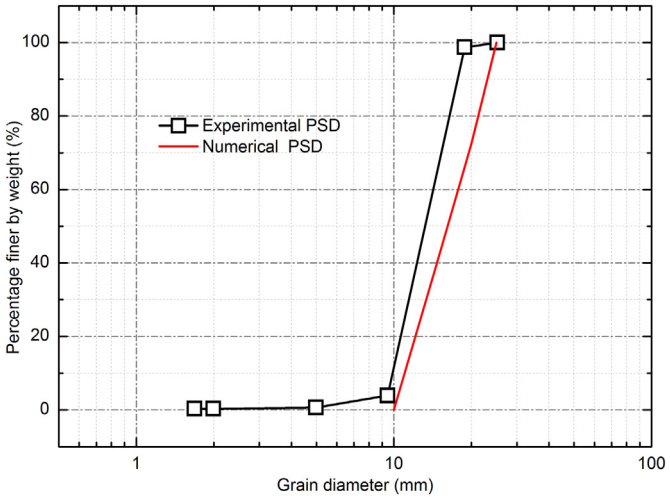

Fig. 3. Particle size distribution of the debris materials used in the experiments (Jiang and Towhata (2013)) and numerical simulations.

2.3. Model validation

The proposed DEM model of flume test has been validated by comparing the numerical results with the experimental data reported in Jiang and Towhata, 2013, regarding the debris flow morphology and impact force. Fig. 4 illustrates that the debris flow morphology in numerical simulations (Fig. 4 (b1–b6)) can approximately match the experimental results (Fig. 4 (a1–a6)). During the tests, the debris motion can be categorized into four stages. In the first stage (see Fig. 4 (a2) and (b2)), the frontal trigger gate was removed and the debris mass started to collapse (Fig. 4 (a2) and (b2)). Then, in the second stage, with the ongoing sliding, the rear section of the debris mass departed from its original location (Fig. 4 (a3) and (b3)) and the frontal debris mass became a thin layer. The middle section experienced less perturbation with small deformation. In the third stage, the debris front hit the rigid barrier and rebounded. Meanwhile, part of the debris mass started to deposit behind the barrier wall at the bottom end of the flume (Fig. 4 (a4) and (b4)). In the last stage, an increasing amount of incoming debris mass arrived and moved onto the deposited debris until the arrest of granular motion for all particles (Fig. 4 (a5) and (b5)). The final deposition is shown in Fig. 4 (a6) and (b6).

The evolution of normal impact force exerted by debris materials on

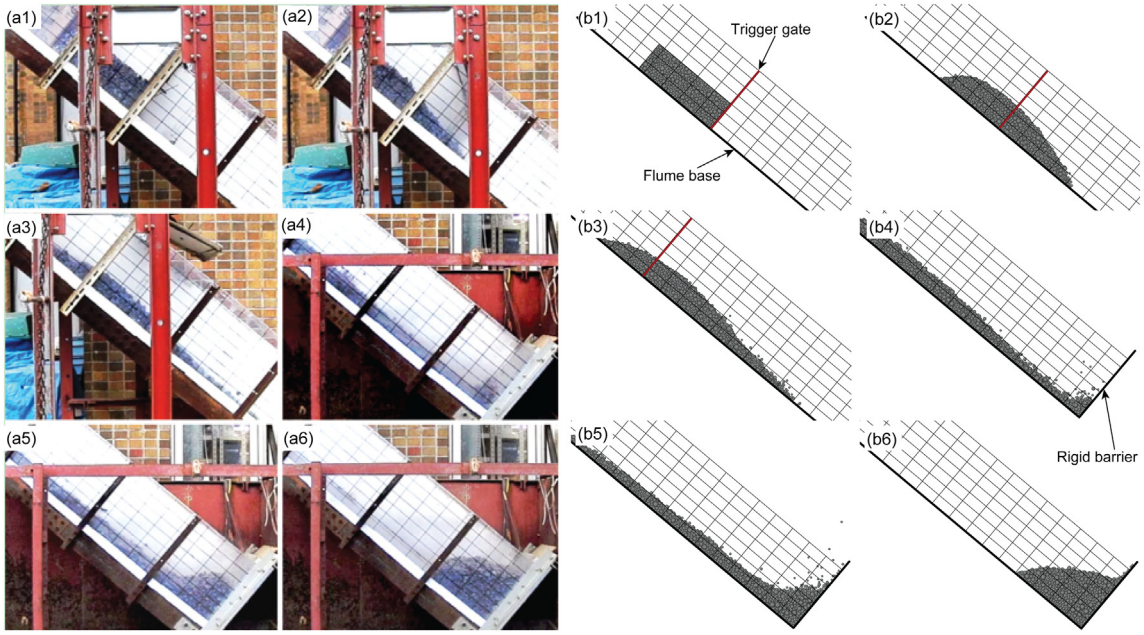

Fig. 4. Snapshots of debris flow impact process (θ = 50°) in the experimental (a1–a6) (Jiang and Towhata (2013)) and numerical (b1–b6) tests. Reference grids (10 × 5 cm) are plotted on the lateral side wall to measure the relative location of debris materials. In numerical simulations, the location of trigger gate is marked as a solid red line. (For interpretation of the references to colour in this figure legend, the reader is referred to the web version of this article.)

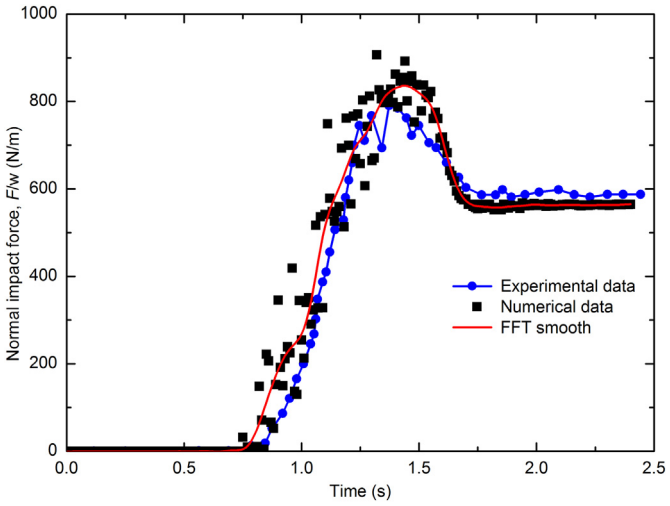

Fig. 5. Evolution of normal impact force in the experimental and numerical tests (θ = 50°).

the barrier is shown in Fig. 5. It can be observed that the numerical results can match well the experimental measurements. In particular, the numerical simulation can capture the characteristics of peak and residual impact forces observed in experiments. It should be noted that the agreement of residual force also indicates that the final debris depositions in both the numerical and experimental tests should have approximately the same shape (see Fig. 4 (a6) and (b6)). This is because the residual force is effectively determined by the geometry of final debris deposition shape (Jiang and Towhata, 2013). In the analyses, the Fast Fourier Transformation (FFT) function is also used to smooth the numerical data. It is apparent that the FFT transformation can represent the general trend of the impact force evolution.

A more detailed quantitative comparison between the numerical and experimental results is shown in Table 2, regarding the velocity (v), depth (h) and Froude number (Fr) of the debris flow at the peak force time. In the analyses, the Froude number is used to characterize the debris flow regime, defined as $Fr = v/\sqrt{gh}$, with g being the gravitational acceleration. It can be seen that the debris flow velocity, depth and Froude number in the simulation are 4.8 m/s, 3.5 cm and 8.2, respectively. These values are very close to the experimental results. According to Iverson (2015), the Froude number is a key parameter governing the debris flow dynamics in an inclined flume. Therefore, the agreement of Froude number between the numerical and experimental results indicate that the DEM model can effective reproduce the fundamental flow characteristics of real debris flows.

Table 2
Fundamental flow characteristics of debris flow at peak force time for numerical simulation and experimental test.

Quantity	Frontal velocity, v (m/s)	Depth, h (cm)	Froude number, Fr
Simulation	4.8	3.5	8.2
Experiment	4.1	3.9	6.7

3. Numerical results

3.1. Dynamics of debris-barrier interaction

In this section, the general features of debris flow impacting on a rigid barrier of θ = 50° are illustrated. Fig. 6 shows the evolution of granular profiles during the impacting process. For visualization purpose, the granular mass has been divided into five sections (S_1, S_2, S_3, S_4 and S_5) at a time instance just before the impact (t = 0.7 s). Each section contains the same number of particles and is set with distinct colors (see Fig. 6 (c)). It can be observed that after the impact, the frontal particles (S_1) are arrested by the barrier forming a thin layer of deposits (see Fig. 6 (c–e)). These deposits can act as a cushion layer for the incoming particles. Thus, particles in the second section can collide onto and climb up over the deposits, reaching the barrier at a high elevation (Fig. 6 (e–f)). Over time, the subsequent incoming debris sections deposit one by one behind the barrier. The final deposition is shown in Fig. 6 (h). Due to the embedding and upward movement of upper flowing particles, the shape of deposited debris layer becomes gradually convex with respect to the barrier.

In order to show the detailed debris-barrier interaction process, a

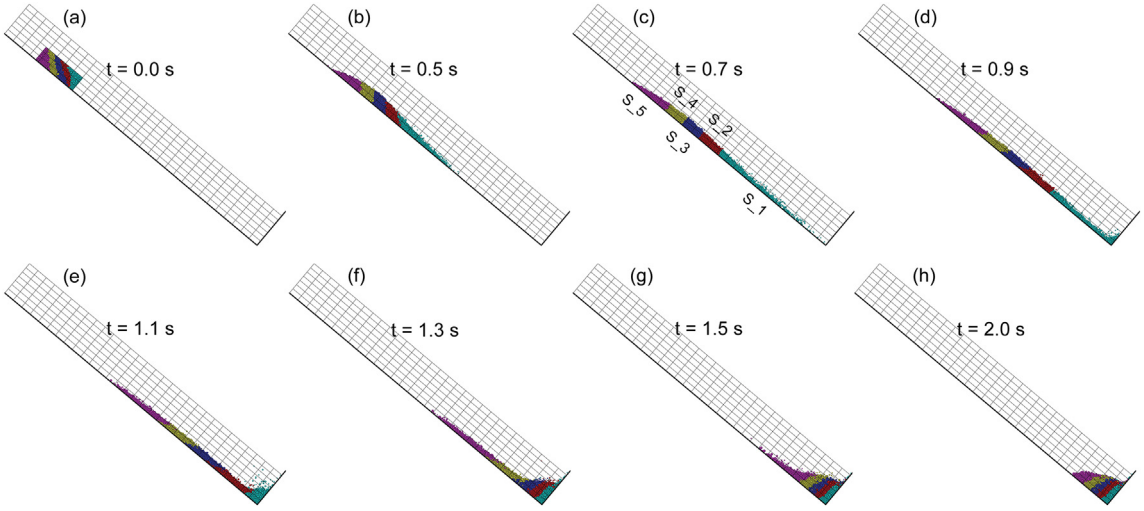

Fig. 6. Evolution of debris motions during the impact against a rigid barrier (θ = 50°). The particles are divided into five equi-numbered sections at t = 0.7 s with distinct colors (cyan, red, blue, yellow and magenta, respectively). (For interpretation of the references to colour in this figure legend, the reader is referred to the web version of this article.)

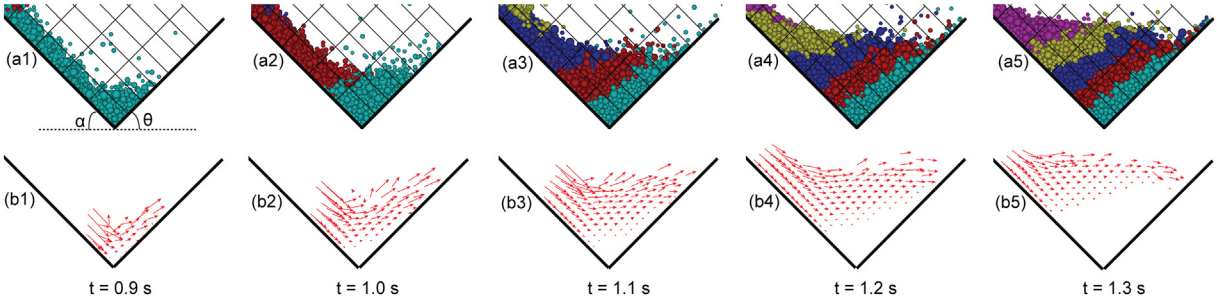

Fig. 7. Snapshots of debris-barrier interactions from t = 0.9 s to t = 1.3 s (θ = 50°). (a1–a5) are the side snapshots of the debris materials. (b1–b5) are the corresponding velocity fields. The length of the arrow is proportional to the velocity magnitude.

side view of granular motions near the rigid barrier (θ = 50°) from t = 0.9 s to t = 1.3 s is presented in Fig. 7 (a1–a5). The corresponding granular velocity fields are shown in Fig. 7 (b1–b5). According to the plots, it can be observed that a small static (deposition) zone exists behind the barrier after the frontal impact between t = 0.9 and t = 1.0 s (see Fig. 7 (b1)). This static zone can impede the debris flow motion leading the subsequent incoming debris to climb onto the static zone with reduced dynamics (see Fig. 7 (b2–b4)). Meanwhile, as the volume of deposited mass increases, the static zone gradually extends to the upstream regions. After some time, the incoming debris materials cannot run over the static granular deposits (see Fig. 7 (b5)) and the run-up height of the debris flow on the barrier reaches the peak value (see Fig. 7 (a4) and (a5)). After that, debris materials in the rear section can only impact and pile up on the existing deposits increasing the total deposits volume. The evolutions of debris deposition, frontal impact, run-up and pile-up have also been observed in some laboratory experiments (Choi et al., 2015; Koo et al., 2017; Ng et al., 2017a; Ng et al., 2017b) and numerical simulations (Law, 2015). Actually, the formation of a static debris deposition zone behind the barrier after the frontal impact has been recognized as the main reason of energy dissipation for the subsequent debris flows (Ashwood and Hungr, 2016; Koo et al., 2017; Ng et al., 2017b).

To analyze the debris motion, the linear momentum of particles in each section was investigated. In fact, measurements of linear momentum have already been proved valuable to characterize the motion of granular materials (Utili et al., 2015). In the current analyses, the linear momentum (P_i) of i-th section can be decomposed into components normal (P_{in}) and tangential (P_{it}) to the barrier as,

$$\begin{cases} P_{in} = \sum_{j=1}^{N} [P_{jx}\sin(\theta) - P_{jy}\cos(\theta)] \\ P_{it} = \sum_{j=1}^{N} [P_{jx}\cos(\theta) + P_{jy}\sin(\theta)] \end{cases} \quad (0^{\circ} < \theta \le 90^{\circ}) \tag{8}$$

where N is the number of particles in the i-th section; P_{jx} and P_{jy} are the momentum components of particle j in x and y directions, respectively.

Fig. 8 shows the evolution of momentum components during a simulation of θ = 50°. Before impact (t < 0.7 s), the tangential momentum component (P_{it}) of each section is nil because the linear momentum (P_i) is perpendicular to the barrier. After the debris flow reaches the barrier (t = 0.8 s), P_{1t} increases slowly as the debris materials gradually pile up behind the barrier. Meanwhile, the normal momentum component (P_n) of S_1 increases slightly to reach the peak value, then decreases gradually to zero. In this process, the rigid barrier changes the flow direction, which makes the granular materials in S_1 to climb up onto the barrier (see Fig. 7 (b2)). For the second section (S_2), P_{2n} reaches the peak value of 16.8 kgm/s at t = 1.1 s, then it decreases gradually to nil due to the interactions with the deposited particles in S_1. Similar to P_{1t}, P_{2t} firstly increases to the maximum value as the debris materials climbing onto the deposits in S_1 (see Fig. 7 (a3)). Then, it decreases slowly to zero due to intensive inter-particle collision and friction. The momentum evolution patterns of S_3, S_4 and S_5 are similar to that of S_2. In these processes, the incoming debris materials can climb onto the previous deposits, changing the tangential momentum.

In the analyses, the barrier was divided into six segments from the bottom to the top regions (indexed as No. 1 to No. 6), as shown in

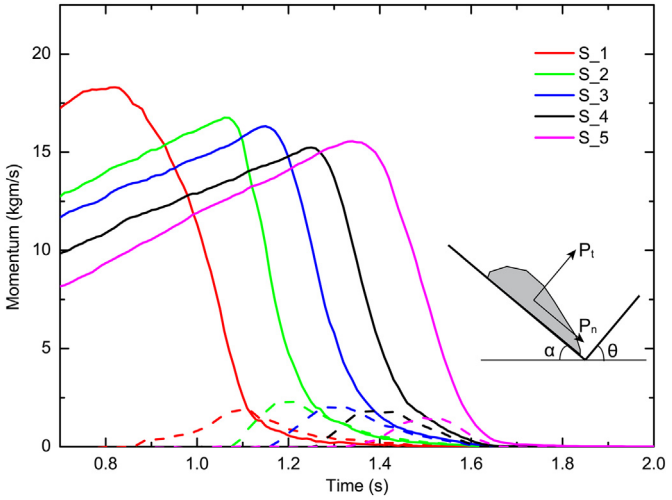

Fig. 8. Evolution of momentum components of five debris sections during a simulation of θ = 50°. P_n is the momentum component normal to the barrier (solid lines). P_t is the momentum component in the tangential direction of the barrier (dashed lines).

Fig. 9(a). The height of the sixth segment is 15 cm which is much larger than that of the other five segments (5 cm), because quite few particles can reach the upper barrier region. The evolution of normal impact force (F_1–F_6) acting on each segment during the simulation is shown in Fig. 9(b). In this figure, the peak values of the normal impact forces are also marked near the curves (F_{1max}, F_{2max}, F_{3max}, F_{4max}, F_{5max} and F_{6max}). As shown in Fig. 9(b), after the debris flow reaches the barrier (t = 0.7 s), the impact forces acting on each barrier segment firstly increase to the peak value and then decrease to the residual stable value. From the bottom to the upper segments, a time delay exists for the emergence of impact force and the corresponding peak value. Since the debris flow cannot climb up to the No. 6 segment (see Fig. 6 (h)), the normal force acting on this segment is almost nil throughout the simulation. In addition, it can be seen that the peak impact force decreases gradually from the bottom to the top of the barrier. This decreasing trend is related to the reduced dynamics of incoming debris particles when they climb onto the existing deposits behind the barrier. From Fig. 9, a non-linear distribution of residual forces with depth can be observed. For example, the residual force of F_2 is nearly the same as that of F_1. According to Jiang and Towhata (2013), this is attributed to the formation of an arch-like protective debris layer behind the barrier.

Analyses of the energy components of the debris flow are important for a comprehensive understanding of the interaction process between the debris flow and rigid barrier. The total energy (E_T) of the granular system consists of potential energy (E_P), kinetic energy (E_K), elastic strain energy (E_S) and the energy loss due to friction (E_F) and local contact viscous damping (E_D). The potential energy (E_P) is defined with respect to the toe of the flume as,

$$E_P = \sum_{i=1}^{N} m_i g H_i \tag{9}$$

where N is the total number of debris particles; m_i and H_i are the mass and height of particle i, respectively. In addition, before release, E_P also corresponds to the total energy of the system, E_0. The kinetic energy (E_K) of the debris flow is calculated as the summation of the translational and rotational kinetic energy of all debris particles.

$$E_K = \frac{1}{2}\sum_{i=1}^{N}\left(m_i\ |v_i|^2 + I_i\ |\omega_i|^2\right) \tag{10}$$

where $I_i = 0.4 m_i r_i^2$ is the momentum of inertia; r_i is the particle radius; v_i and ω_i are the translational and rotational velocities, respectively.

The elastic strain energy (E_S) is the energy stored in the normal and tangential contacts, which can be expressed as,

$$E_S = \frac{1}{2}\sum_{i=1}^{N_c}\left(\frac{|F_i^n|^2}{k_i^n} + \frac{|F_i^s|^2}{k_i^s}\right) \tag{11}$$

where N_c is the number of contacts; F_i^n and F_i^s are the normal and shear forces; k_i^n and k_i^s are the normal and shear stiffness, respectively.

The energy loss due to friction (E_F) occurred after the shear failure between any two spherical particles can be expressed as,

$$E_F^j = E_F^{j-1} + \sum_{i=1}^{N_c}\left(F_i^s\left(\Delta u_i^s - (\Delta u_i^s)^{elastic}\right)\right) \tag{12}$$

where E_F^j and E_F^{j-1} are the cumulative energy loss by friction at the current and previous time steps; Δu_i^s is the total incremental shear displacement; $(\Delta u_i^s)^{elastic}$ is the shear displacement related to the incremental shear force.

The energy loss by viscous damping at contact (E_D) is computed by the viscous dashpot model as,

$$E_D^j = E_D^{j-1} + \sum_{i=1}^{N_c}\left(|F_i^n \Delta u_i^n|\right) \tag{13}$$

where E_D^j and E_D^{j-1} are the cumulative energy loss by damping at the current and previous time steps; Δu_i^n is the incremental normal displacement.

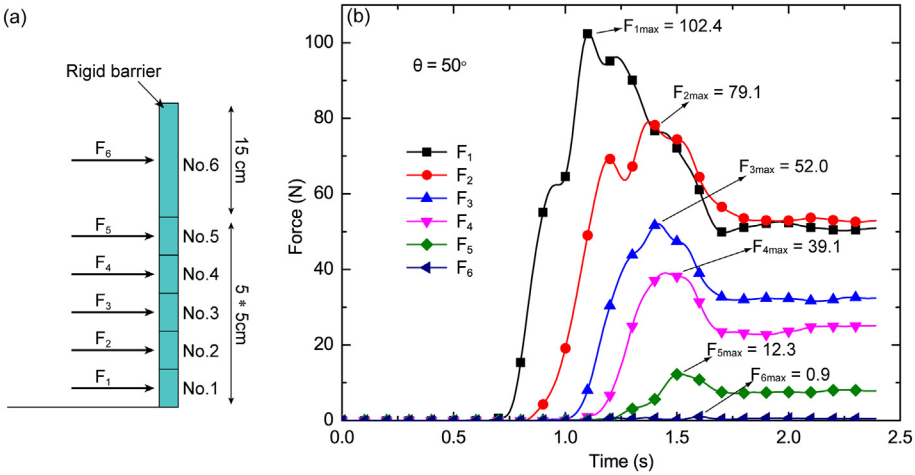

Fig. 9. (a) Rigid barrier division from the bottom to the top. (b) Evolution of normal impact forces on the rigid barrier (θ = 50°). Zero time corresponds to the time instance at which the granular mass is released.

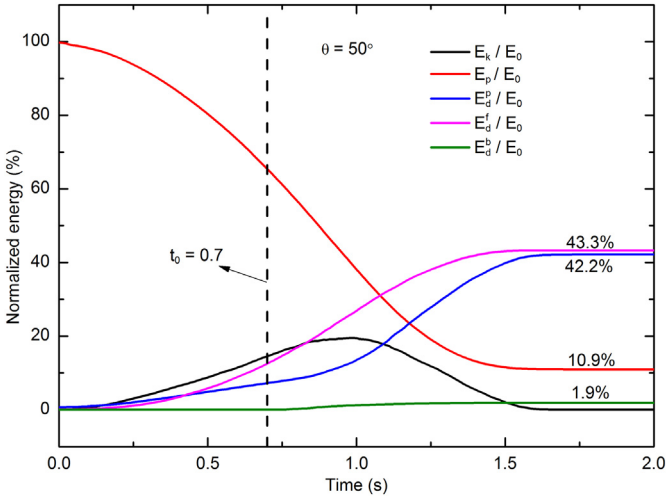

Fig. 10. Evolution and transformation of debris energy during a simulation of θ = 50°. The vertical dashed line indicates the arrival time of granular flow at the barrier. All energy components are normalized by the initial gravitational potential energy (E_0).

All these energy components can be recorded during the simulations and subsequently analyzed regarding the energy evolution and transformation, as shown in Fig. 10. In this study, the energy dissipated by friction at the flume base (E_d^f), rigid barrier (E_d^b) and inter-particle interaction (E_d^p) were recorded separately. The strain energy (E_S) is not plotted since its value is negligibly small. As shown in Fig. 10, the debris flow involves a cascade of energy evolution which begins at debris flow initiation and ends at deposition. As the granular materials flow downslope, the gravitational potential energy decreases gradually. A portion of the reduced energy transforms into the kinetic energy, increasing the debris velocity. The remainder input energy is dissipated by the flume friction, grain contact friction and inelastic collisions. At impact (t_0 = 0.7 s), a small portion of granular energy is dissipated due to friction and damping arisen from debris-barrier interactions (E_d^b). The subsequent interactions between the incoming and deposited debris materials will further reduce the granular dynamics and thus increase the energy loss. Finally, E_k reduces to 0 and around 90% of initial total energy has been dissipated. In particular, the energy dissipated by rigid barrier (E_d^b) only amounts to 1.9% of E_0, while it can be > 85% by particle-particle and particle-flume interactions. The numerical results indicate that the majority of the initial total energy is not dissipated by particle collisions on rigid barrier, but by inter-particle and particle-flume interactions during the propagation and deposition stages of debris flow. However, the debris-barrier interaction can facilitate the deposition of debris materials behind the barrier, forming a loose granular layer to absorb the kinetic energy of subsequent approaching debris. This finding is in agreement with the experimental observations in Ashwood and Hungr (2016), Ng et al. (2017b) and Koo et al. (2017).

3.2. Influence of barrier slope

As discussed above, several laboratory flume tests and numerical simulations have been conducted to investigate debris-barrier interactions with the barrier perpendicular to the flume. In fact, the barrier slope has a great influence on the debris-barrier interactions (Chu et al., 1995; Mancarella and Hungr, 2010). It affects the run-up height and deposition characteristics of debris flows, because the collision angle of particles onto the barrier can affect the debris deceleration and momentum transformation significantly (Chu et al., 1995). Therefore, it is also necessary to investigate the influence of barrier slope on the debris-barrier interactions. This section presents numerical results of tests with barrier slope (θ) varying from 30°, 50°, 70° and 90° to the horizontal, while the slope inclination angle remains constant (α = 40°).

Fig. 11 shows the final depositions of debris particles behind the barrier for simulations with various barrier slopes. The effective run-up height (H_e) and spreading distance (L_s) of the debris flow is labeled in the figure. In case of gentle barrier slopes (θ ≤ 50°), the first section of the debris is convex in the final deposition, while for steeper barrier slopes, it becomes a wedged shape. Indeed, the convex deposition of particles exhibits very high resistance, which can effectively reduce the subsequent dynamics of the incoming debris materials. As the barrier slope increases, the spreading distance of S_1 decreases. For the test of θ = 30°, the first section can reach the No. 6 segment of the barrier (see Fig. 11 (b1)). Nevertheless, for the test of θ = 90°, the first section can only reach the No. 4 segment (see Fig. 11 (b4)). As the barrier slope increases, the number of granular sections interacting with the barrier also increases. As shown in Fig. 11 (b1–b4), the steeper the barrier is, the more particles in S_2 can reach the barrier. For the test of θ = 90°, particles in the third section (S_3) can also reach the barrier (Fig. 11 (b4)).

Fig. 12 shows the evolutions of normal (P_n) and tangential (P_t) momentum components of each section during simulations of various barrier slopes. It is apparent that before impact, at gentle barrier slopes (θ ≤ 50°), P_t is positive, while at steep barrier slopes (θ > 50°), P_t is negative. In addition, the initial value of P_t is nil for the case of barrier being perpendicular to the slope (θ = 50°). According to Fig. 12, the normal momentum component generally increases approximately linearly to the peak value (either positive or negative) and then decreases gradually to zero. For test of θ = 30°, the tangential momentum component keeps positive during the whole process of debris flow. After the peak, P_t decreases gradually to zero. Due to the positive momentum component, the debris particles in S_1 can spread to a long distance and reach a large height behind the barrier (see also Fig. 11 (a1) and (b1)). For tests of θ > 50°, P_t keeps negative, indicating that the momentum component contributes little to the spreading of debris materials. In particular, the spreading distance of the first section is obviously

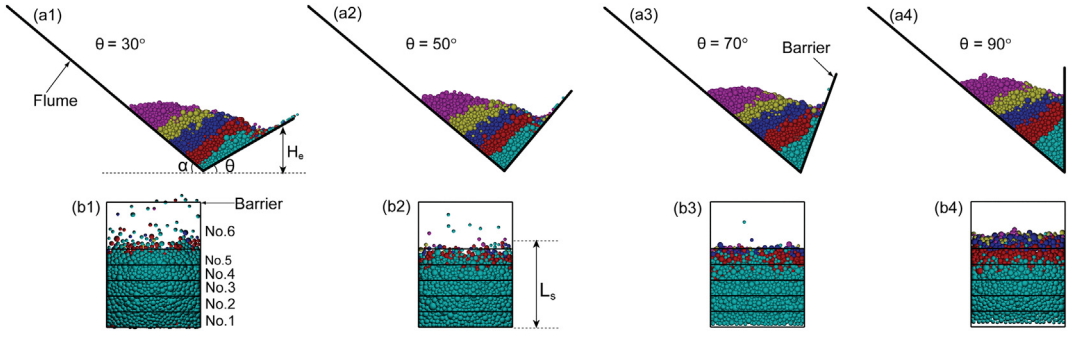

Fig. 11. Side view of the final debris deposition (a1–a4) and distribution of particles behind the barrier (b1–b4) (view from the direction perpendicular to the barrier) for simulations with various barrier slopes.

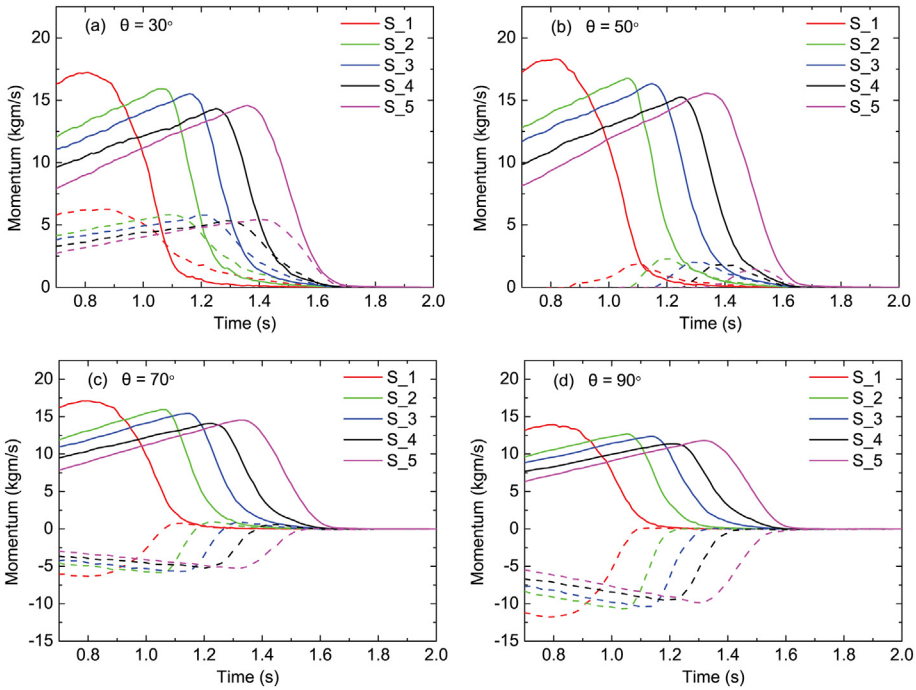

Fig. 12. Evolution of normal (P_n, solid lines) and tangential (P_t, dashed lines) debris momentum components for tests of various barrier slopes.

shorter than that in tests of θ < 50° (see Fig. 11). Therefore, as the barrier slope decreases, the spreading distance of the first section increases due to the positive tangential momentum component. However, the number of particles in S_2 reaching the barrier decreases due to intensive particle interactions with the S_1 deposits (see Fig. 11).

Based on the normal forces recorded in each barrier segment, the total normal force (F) acting on a barrier can be calculated as,

$$F = \sum_{i=1}^{6} F_i \tag{14}$$

Fig. 13 shows the evolution of total normal impact force acting on the rigid barrier for tests of various barrier slopes. After the debris flow reaches the barrier (t > 0.7 s), the impact force increases quickly to the peak value. Then, it decreases gradually to a residual stable value which is related to the earth pressure of the final deposition. The maximum impact force (F_{max}) increases with the barrier slope.

In engineering practice, the maximum impact force (F_{max}) is commonly evaluated via the hydrodynamic approach (Kwan, 2012) as,

$$F_{max} = \kappa\rho v^2 hw \sin(180^{\circ}\text{-}\alpha\text{-}\theta) \tag{15}$$

where κ is the dynamic pressure coefficient; ρ is the density of the flow (kg/m^3); v is the frontal velocity; h is the flow depth (m); w is the barrier width (m), α is the flume inclination angle (40° in this study). The dynamic pressure coefficient is a function of the Froude number (Fr), which is expressed as,

$$\kappa = aFr^b \tag{16}$$

where a and b are two empirical coefficients. In this study, the dynamic pressure coefficient is calculated by the empirical formula proposed by Jiang and Towhata (2013) with a = 10.8 and b = −1.3.

According to Eq. (15), when the barrier slope (θ) equals to 50°, the maximum impact force F_{max} (see the definition in Fig. 13) can reach the peak value, because in this case, the flow velocity is perpendicular to the barrier (see the theoretical results in Fig. 14). However, as shown in

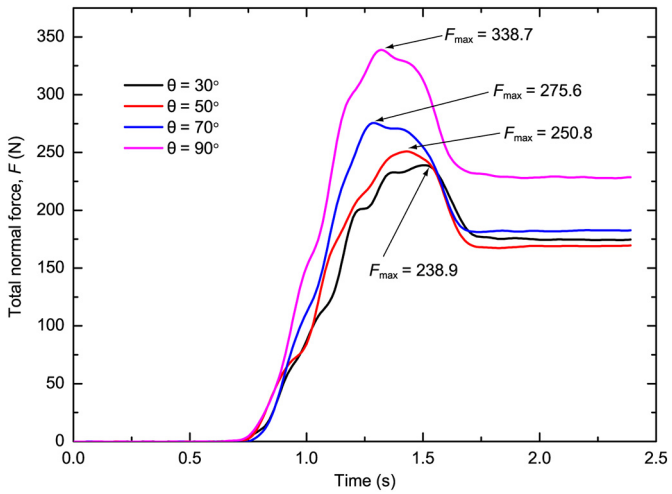

Fig. 13. Evolution of total normal impact force acting on the rigid barrier for tests of various barrier slopes.

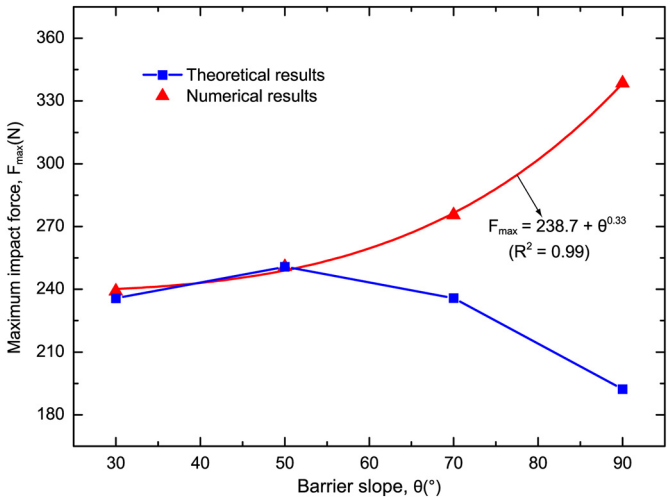

Fig. 14. Relationship between the maximum impact force and the barrier slope. The theoretical results are evaluated by the hydrodynamic approach.

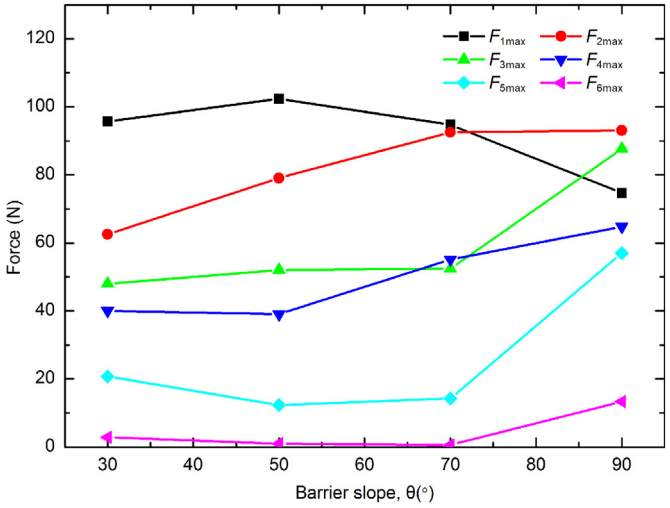

Fig. 15. Maximum impact forces acting on the six segments of the barrier at different barrier slope.

Fig. 14, in the DEM results, F_{max} increases with the barrier slope, following a power law relationship. The mismatch of numerical and theoretical results can be attributed to the impacting process of debris flow originating from the microscopic particle-barrier interactions. A detailed discussion will be given in the following sections.

As a detailed comparison, the maximum impact force acting on each segment (e.g., F_{1max} to F_{6max}) for different barrier slopes are plotted in Fig. 15. In the plot, F_{imax} denotes the maximum impact force acting on the i-th segment of the barrier. As shown in Fig. 15, for the first segment, F_{1max} increases to the peak value at $\theta = 50^{\circ}$ and then decreases to a minimum value at $\theta = 90^{\circ}$. This indicates that the relationship between F_{1max} and the barrier slope can follow well the hydrodynamic formula. However, for the second, third and fourth segments, the maximum impact forces (i.e. F_{2max}, F_{3max}, F_{4max}) increase with the barrier slope. F_{5max} and F_{6max} tend to decrease slightly as the barrier slope angle increases from 30° to 70°, while they increase quickly for larger barrier slope angles and reach the peak values at $\theta = 90^{\circ}$. Therefore, it is the increasing pattern of F_{2max} to F_{6max} that can finally lead to the increase of the overall maximum total impact force (F_{max}) with the barrier slope (see Fig. 14).

As discussed before, at a gentle barrier slope (e.g. $\theta = 30^{\circ}$), the interface of successive granular deposition layers is curved (see Fig. 11 (a1)), while it becomes gradually flat at steeper barrier slopes (see Fig. 11 (b1)). The curved deposition surface would increase the sliding distance of overlaying granular materials with intensive particle-particle interactions, leading to relatively low debris impacting velocity and force on the barrier. As shown in Fig. 16, the impacting velocity of the debris particles on the barrier wall increases with the barrier slope. In addition, as the barrier slope increases, the angle between the impacting velocity and the rigid barrier would increase accordingly (see Fig. 16). Meanwhile, the spreading distance of the debris flow front (i.e. S_1) decreases, such that the incoming granular materials can impact on the barrier directly (see Fig. 11). For tests of gentle barrier slopes, the incoming debris materials can have intensive interactions with the pre-deposited grains due to long spreading distance, dissipating a considerable amount of kinetic energy. As a result, very little or none of the incoming debris materials can reach the barrier slope. This process can greatly reduce the impact force of the incoming debris materials on the rigid barrier.

The obtained numerical results indicate that the barrier slope angle is an important factor that should be considered in the design of a rigid barrier. At gentle barrier slopes ($\theta \leq 50^{\circ}$), the spreading distance of the debris flow front is relatively long due to the positive momentum component in the tangential direction of the barrier (see the discussion on Fig. 12). On the contrary, at steep barrier slopes ($\theta > 50$), the spreading distance is relatively short due to the negative momentum component. Given that the deposited debris materials behind the barrier would exert friction and damping on the overlaying sliding debris materials, it can be concluded that deposits of long spreading distance are very effective in facilitating energy dissipation of debris flows, which diminishes the impact force acting on the barrier. This result also suggests that the rigid barrier of steep slope is more vulnerable than the gentle ones. Therefore, a higher dynamic pressure coefficient in Eq. (16) should be adopted in preliminary designs of a rigid barrier with steep slope.

4. Discussion

4.1. Model scale effect

As the current DEM model of flume test has relatively smaller dimensions than real natural debris flows, it is necessary to investigate the potential influence of model size on the behavior of debris-barrier interactions. In particular, when applying the current numerical study to filed work, the problem would arise immediately as to what extent the small-scale simulations are representative of field observations. According to Valentino et al. (2007) and Jiang and Towhata (2013), the flume experiment can be considered as a two-dimensional representation of real debris flows, which should be configured to obtain a systematical dynamic similarity to the prototype. According to Buckingham's Π theorem, two dimensionless parameters, d/h and Froude number ($Fr = v/\sqrt{gh}$) should be identical in both small-scale model test and the corresponding prototype (d is the mean particle diameter; h is flow depth and v is the flow front velocity). From Table 1 and Table 2, it can be calculated that d/h is 0.5 and Fr is 8.2. Therefore, the numerical model in this study can be considered identical to a type of dry debris flows with d/h being equal to 0.5 and Fr being equal to 8.2.

4.2. Fluid effect

In this study, the interactions between dry debris flows and a rigid barrier are investigated. Actually, the fluid plays a vital role in all debris flows and many other landslides (Iverson, 2015). The interaction between the fluid phase and solid phase can lead to very complex flow dynamics. Song et al. (2016) investigated the influence of water content on the impact of debris flows against a rigid barrier. Their results indicate that the Froude number (Fr) of debris flow increases with the water content. The variation of Fr gives rise to different mechanisms of debris-barrier interactions. For tests of high water content (> 50%), the debris barrier interaction process is dominated by the run-up mechanism. On the contrary, the dry debris flow exhibits a predominant pile-up mechanism. As shown in Fig. 6, the interaction process is dominated by the pile-up mechanism, which is in accordance with the experimental results of Song et al. (2016). Therefore, the results of this study can still give some new insights into the interactions between dry debris flows and a rigid barrier.

5. Conclusions

The impact of a dry debris flow onto a rigid barrier has been analyzed via a numerical flume test using the open source DEM code ESyS-Particle. This model was validated by comparing the numerical results with the experimental testing data under the same model configurations. The validated model was then used to investigate the influence of barrier slope on debris-barrier interactions. The obtained numerical results revealed the characteristics of flow-barrier interactions, with the potential applications to a rigid barrier design.

Based on the numerical modeling, three key interaction stages, namely the frontal impact, run-up and pile-up were identified. These stages are in good agreement with the experimental and numerical

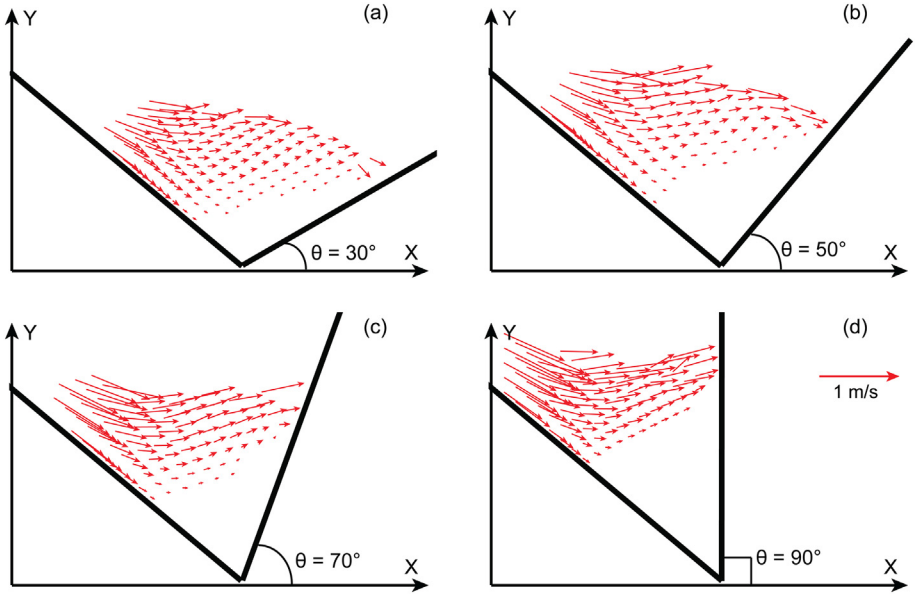

Fig. 16. Velocity fields at the time instance corresponding to the peak impact force at different barrier slopes.

observations reported in the literature. The frontal impact stage is characterized by the formation of an initial static debris zone. The run-up stage involves the flowing debris materials climbing up onto the deposits of the flow front. The pile-up stage is featured by the progressive increase of deposit volume with no debris materials colliding onto the barrier. In addition, the analyses of energy transformation show that > 85% of the initial total energy of the debris system was dissipated by particle-particle and particle-flume interactions, while only 2% by particle-barrier interactions. The results also indicate that the maximum impact force increases with the barrier slope, following a power law relationship, which is not in accordance with the prediction by the hydrodynamic formula as commonly used in engineering practices. This conventional formula can predict well the impact force under the condition that the barrier is perpendicular to the slope. However, for a steeper barrier slope, the formula would underestimate the maximum impact force. Thus, more robust theories of debris-barrier interactions need to be established based on a large amount of numerical, experimental and field investigations.

Acknowledgements

This research was supported by the National Natural Science Foundation of China (grants 51639007 and 41602289) and the Fundamental Research Funds for the Central Universities (grant 2017SCU04A09). JZ acknowledges the financial supports provided by Research Grants Council of Hong Kong through a Theme-based Research Project (No. T22-603/15N) and a Collaborative Research Fund project (Grant No. C6012-15G).

References

Albaba, A., Lambert, S., Nicot, F., Chareyre, B., 2015. Relation between microstructure and loading applied by a granular flow to a rigid wall using DEM modeling. Granul. Matter 17 (5), 603–616.
Ashwood, W., Hungr, O., 2016. Estimating the total resisting force in a flexible barrier impacted by a granular avalanche using physical and numerical modeling. Can. Geotech. J. 53 (10), 1700–1717.
Brighenti, R., Segalini, A., Ferrero, A.M., 2013. Debris flow hazard mitigation: a simplified analytical model for the design of flexible barriers. Comput. Geotech. 54, 1–15.
Calvetti, F., Crosta, G., Tatarella, M., 2000. Numerical simulation of dry granular flows: from the reproduction of small-scale experiments to the prediction of rock avalanches. Rivista Italiana Di Geotecnica 2 (2), 21–38.
Calvetti, F., di Prisco, C.G., Vairaktaris, E., 2017. DEM assessment of impact forces of dry granular masses on rigid barriers. Acta Geotech. 12 (1), 129–144.
Chen, X., Cui, P., You, Y., Chen, J., Li, D., 2015. Engineering measures for debris flow hazard mitigation in the Wenchuan earthquake area. Eng. Geol. 194 (Supplement C), 73–85.
Choi, C.E., Au-Yeung, S.C.H., Ng, C.W.W., Song, D., 2015. Flume investigation of landslide granular debris and water runup mechanisms. Géotech. Lett. 5 (1), 28–32.
Chu, T., Hill, G., Mcclung, D.M., Ngun, R., Sherkat, R., 1995. Experiments on granular flows to predict avalanche runup. Can. Geotech. J. 32 (2), 285–295.
Cundall, P.A., Strack, O.D.L., 1979. A discrete numerical model for granular assemblies. Geotechnique 29 (1), 47–65.
Fan, R.L., Zhang, L.M., Wang, H.J., Fan, X.M., 2018. Evolution of debris flow activities in Gaojiagou Ravine during 2008–2016 after the Wenchuan earthquake. Eng. Geol. 235, 1–10.
Gabrieli, F., Ceccato, F., 2016. Impact of dry granular flows on a rigid wall: discrete and continuum approach. Procedia Eng. 158, 152–157.
Gao, G., Meguid, M.A., 2018. On the role of sphericity of falling rock clusters—insights from experimental and numerical investigations. Landslides 15 (2), 219–232.
Gao, L., Zhang, L.M., Chen, H.X., 2017. Two-dimensional simulation of debris flow impact pressures on buildings. Eng. Geol. 226 (Supplement C), 236–244.
Hungr, O., 1995. A model for the runout analysis of rapid flow slides, debris flows, and avalaches. Can. Geotech. J. 32 (4), 610–623.
Hürlimann, M., Copons, R., Altimir, J., 2006. Detailed debris flow hazard assessment in Andorra: a multidisciplinary approach. Geomorphology 78 (3), 359–372.
Iverson, R.M., 2015. Scaling and design of landslide and debris-flow experiments. Geomorphology 244, 9–20.
Jiang, Y.J., Towhata, I., 2013. Experimental study of dry granular flow and impact behavior against a rigid retaining wall. Rock Mech. Rock Eng. 46 (4), 713–729.
Jiang, Y.J., Zhao, Y., Towhata, I., Liu, D.X., 2015. Influence of particle characteristics on impact event of dry granular flow. Powder Technol. 270, 53–67.
Koo, R.C.H., Kwan, J.S.H., Ng, C.W.W., Lam, C., Choi, C.E., Song, D., Pun, W.K., 2017. Velocity attenuation of debris flows and a new momentum-based load model for rigid barriers. Landslides 14, 1–13.
Kwan, J.S.H., 2012. Supplementary technical guidance on design of rigid debris-resisting barriers. Technical Note No.TN 2/2012. Geotech. Eng. Off (Civil Engineering and Development Department, The HKSAR Government).
Kwan, J.S., Sun, H.W., 2006. An improved landslide mobility model. Can. Geotech. J. 43 (5), 531–539.
Law, P.H., 2015. Computational Study of Granular Debris Flow Impact on Rigid Barriers and Baffles. D.Phil. The Hong Kong University of Science and Technology (D.Phil Thesis).
Legros, F., 2002. The mobility of long-runout landslides. Eng. Geol. 63 (3), 301–331.
Liu, J., You, Y., Chen, X., Liu, J., Chen, X., 2014. Characteristics and hazard prediction of large-scale debris flow of Xiaojia Gully in Yingxiu Town, Sichuan Province, China. Eng. Geol. 180, 55–67.
Mancarella, D., Hungr, O., 2010. Analysis of run-up of granular avalanches against steep, adverse slopes and protective barriers. Can. Geotech. J. 47 (8), 827–841.
Moriguchi, S., Borja, R.I., Yashima, A., Sawada, K., 2009. Estimating the impact force generated by granular flow on a rigid obstruction. Acta Geotech. 4 (1), 57–71.
Ng, C.W.W., Choi, C.E., Liu, L.H.D., Wang, Y., Song, D., Yang, N., 2017a. Influence of particle size on the mechanism of dry granular run-up on a rigid barrier. Géotech. Lett. 7 (1), 79–89.
Ng, C.W.W., Song, D., Choi, C.E., Liu, L.H.D., Kwan, J.S.H., Koo, R.C.H., Pun, W.K., 2017b. Impact mechanisms of granular and viscous flows on rigid and flexible barriers. Can. Geotech. J. 54 (2), 188–206.
Plassiard, J.P., Donzé, F.V., 2010. Optimizing the design of rockfall embankments with a discrete element method. Eng. Struct. 32 (11), 3817–3826.

Salciarini, D., Tamagnini, C., Conversini, P., 2010. Discrete element modeling of debris-avalanche impact on earthfill barriers. Phys. Chem. Earth 35 (3–5), 172–181.
Shan, T., Zhao, J., 2014. A coupled CFD-DEM analysis of granular flow impacting on a water reservoir. Acta Mech. 225 (8), 2449–2470.
Shen, W.G., Zhao, T., Crosta, G.B., Dai, F., 2017. Analysis of impact-induced rock fragmentation using a discrete element approach. Int. J. Rock Mech. Min. Sci. 98, 33–38.
Song, D., Ng, C.W.W., Choi, C., Zhou, G.D., Kwan, J.S.H., Koo, R.C.H., 2016. Influence of debris flow solid fraction on rigid barrier impact. Can. Geotech. J. 54 (10), 1421–1434.
Utili, S., Zhao, T., Houlsby, G.T., 2015. 3D DEM investigation of granular column collapse: evaluation of debris motion and its destructive power. Eng. Geol. 186, 3–16.
Valentino, R., Barla, G., Montrasio, L., 2007. Experimental analysis and micromechanical modelling of dry granular flow and impacts in laboratory flume tests. Rock Mech. Rock Eng. 41 (1), 153.
Wang, Y., Mora, P., 2009. The ESyS_Particle: a new 3-D discrete element model with single particle rotation. In: Advances in Geocomputing. Springer Berlin Heidelberg, Berlin, Heidelberg, pp. 183–228.
Wu, F., Fan, Y., Liang, L., Wang, C., 2016. Numerical simulation of dry granular flow impacting a rigid wall using the discrete element method. PLoS One 11 (8), 1–17.
Zhao, T., Houlsby, G.T., Utili, S., 2014. Investigation of granular batch sedimentation via DEM-CFD coupling. Granul. Matter 16 (6), 921–932.
Zhao, T., Dai, F., Xu, N.W., Liu, Y., Xu, Y., 2015. A composite particle model for non-spherical particles in DEM simulations. Granul. Matter 17 (6), 763–774.
Zhao, T., Utili, S., Crosta, G.B., 2016. Rockslide and impulse wave modelling in the Vajont reservoir by DEM-CFD analyses. Rock Mech. Rock. Eng. 49 (6), 2437–2456.
Zhao, T., Crosta, G.B., Utili, S., De Blasio, F.V., 2017a. Investigation of rock fragmentation during rockfalls and rock avalanches via 3-D discrete element analyses. J. Geophys. Res. Earth Surf. 122 (3), 678–695.
Zhao, T., Dai, F., Xu, N., 2017b. Coupled DEM-CFD investigation on the formation of landslide dams in narrow rivers. Landslides 14 (1), 189–201.
Zhao, T., Crosta, G., Dattola, G., Utili, S., 2018. Dynamic fragmentation of jointed rock blocks during rockslide-avalanches: insights from discrete element analyses. J. Geophys. Res. Sol. Ea. 123, 1–20.